# Supporting Online Material to the manuscript: "An assessment of diffusion-based temperature proxies."

C. Holme[1], V. Gkinis[1], and B. M. Vinther[1]

[1]Centre for Ice and Climate, Niels Bohr Institute, University of Copenhagen, Juliane Maries Vej 30, DK-2100 Copenhagen, Denmark

## I. Derivation of the integration equations for $\sigma^2$

In this section we show how we derive the numerical expressions for the diffusion length (Eq. (7) in main text). Starting from the differential equation for the diffusion length we have:

$$\frac{\mathrm{d}\sigma^2}{\mathrm{d}t} - 2\,\dot{\varepsilon}_z(t)\,\sigma^2 = 2D(t)\,. \tag{1}$$

We consider the vertical strain rate due to densification:

$$\dot{\varepsilon}_z\,(t) = \frac{-\partial\rho}{\partial t}\,\frac{1}{\rho} \tag{2}$$

We substitute $t$ with $\rho$ and combine Eq.(1), (2) to get:

$$\frac{\mathrm{d}\sigma^2}{\mathrm{d}\rho} + \frac{2\sigma^2}{\rho} = 2\left(\frac{\mathrm{d}\rho}{\mathrm{d}t}\right)^{-1} D(\rho) \tag{3}$$

Multiplying both sides of Eq.3 with the integrating factor

$$F(\rho) = e^{\int \frac{2}{\rho}\mathrm{d}\rho} = \rho^2, \tag{4}$$

we get:

$$\frac{\mathrm{d}}{\mathrm{d}t}\left(\rho^2\sigma^2\right) = 2\rho^2\left(\frac{\mathrm{d}\rho}{\mathrm{d}t}\right)^{-1} D(\rho), \tag{5}$$

from which we get the result:

$$\sigma^2\,(\rho) = \frac{1}{\rho^2}\int_{\rho_o}^{\rho} 2\rho^2\left(\frac{\mathrm{d}\rho}{\mathrm{d}t}\right)^{-1} D(\rho)\;\mathrm{d}\rho. \tag{6}$$

In a similar way for the ice diffusion length (Eq. (12) in the main text) we have:

$$\frac{\mathrm{d}\sigma^2}{\mathrm{d}t} - 2\,\dot{\varepsilon}_z(t)\,\sigma^2 = 2D(t)\,, \tag{7}$$

where the total thinning is given by:

$$\mathcal{S}\left(t'\right) = e^{\int_0^{t'}\dot{\varepsilon}_z(t)\mathrm{d}t}\;. \tag{8}$$

We multiply both sides of Eq. (7) with the integrating factor

$$F(\rho) = e^{\int_0^{t'} -2\dot{\varepsilon}_z(t)\mathrm{d}t}, \tag{9}$$

which results in

$$\frac{\mathrm{d}}{\mathrm{d}t}\left[\sigma^2 e^{\int_0^{t'} -2\dot{\varepsilon}_z(t)\mathrm{d}t}\right] = 2D(t)e^{\int_0^{t'} -2\dot{\varepsilon}_z(t)\mathrm{d}t}, \tag{10}$$

and gives the expression for the calculation of the ice diffusion length

$$\sigma^2_{ice}\big(t'\big) = S\big(t'\big)^2\int_0^{t'} 2D_{ice}(t)\,S(t)^{-2}\;\mathrm{d}t. \tag{11}$$

## II. THE DIFFUSIVITY PARAMETRIZATION

### A. The firn diffusivity

We used the diffusivity parametrization as introduced by Johnsen et al. (2000).

$$D(\rho) = \frac{m\,p\,D_{ai}}{R\,T\,\alpha_i\,\tau}\left(\frac{1}{\rho} - \frac{1}{\rho_{ice}}\right). \tag{12}$$

The terms used in Eq. (12) and their parameterizations used are described below:

- $m$ is the molar weight (kg)
- $p$: saturation vapor pressure over ice (Pa). We use Murphy and Koop (2005):

$$p = \exp\left(9.5504 - \frac{5723.265}{T} + 3.530\,\ln(T) - 0.0073\,T\right). \tag{13}$$

- $D_a$: diffusivity of water vapor in air ($\mathrm{m^2 s^{-1}}$). We use (Hall and Pruppacher, 1976):

$$D_a = 2.1\cdot 10^{-5}\left(\frac{T}{T_o}\right)^{1.94}\left(\frac{P_o}{P}\right) \tag{14}$$

  with $P_o = 1$ Atm, $T_o = 273.15$ K and $P,\ T$ the ambient pressure (Atm) and temperature (K). Additionally from Merlivat and Jouzel (1979) $D_{a^2\mathrm{H}} = \frac{D_a}{1.0285}$ and $D_{a^{18}\mathrm{O}} = \frac{D_a}{1.0251}$.
- $R$: molar gas constant $R = 8.314478\ \left(\mathrm{m^3 Pa\ (K\,mol)^{-1}}\right)$
- $T$: Ambient temperature (K)
- $\alpha_i$: Ice – Vapor fractionation factor. we use the formulations by Majoube (1971) and Merlivat and Nief (1967) for $\alpha^2_{s/v}$ and $\alpha^{18}_{s/v}$ respectively.

$$\ln\alpha_{Ice/Vapor}\left({}^2\mathrm{H}/{}^1\mathrm{H}\right) = 16288/T^2 - 9.34\times 10^{-2} \tag{15}$$

$$\ln\alpha_{Ice/Vapor}\left({}^{18}\mathrm{O}/{}^{16}\mathrm{O}\right) = 11.839/T - 28.224\times 10^{-3} \tag{16}$$

- $\tau$: The firn tortuosity. We use (Schwander et al., 1988; Johnsen et al., 2000):

$$\frac{1}{\tau} = \begin{cases} 1 - b_\tau\left(\frac{\rho}{\rho_{ice}}\right)^2 & \text{, for } \rho \le \frac{\rho_{ice}}{\sqrt{b}} \\ 0 & \text{, for } \rho > \frac{\rho_{ice}}{\sqrt{b}} \end{cases}, \tag{17}$$

  where $b_\tau = 1.30$, implying a close-off density of $\rho_{\mathrm{co}} = 804.3\ \mathrm{kgm^{-3}}$.

### B. The ice diffusivity

Ice diffusion is believed to occur via a vacancy mechanism with transport of molecules within the ice lattice. Based on isotopic probe experiments, there is a strong consensus that the ice diffusivity coefficient is the same for $\mathrm{H_2}\,{}^{18}\mathrm{O}$, $\mathrm{D_2O}$ and $\mathrm{T_2O}$ (Ramseier, 1967; Blicks et al., 1966; Itagaki, 1967; Delibaltas et al., 1966) The dependence of the ice diffusivity parameter to temperature is described by an Arrhenius type equation

$$D = D_0\exp\left(-Q/RT\right), \tag{18}$$

where $Q$ is the activation energy and $D_0$ a pre-exponential factor. The results of the studies mentioned above agree well with each other and here we plot the diffusivity parametrization coefficients suggested by those studies (Fig. 1). The ice diffusion length calculations in our work use the results of Ramseier (1967) according to which we use $Q = 0.62$ eV and $D_o = 9.2\cdot 10^{-4}\ \mathrm{m^2\,s^{-1}}$. Note that the results of Ramseier (1967) are based on measurements of both artificially as well as naturally grown ice collected at Mendenhall glacier, Alaska.

## III. EXAMPLES OF DIFFUSION LENGTHS FOR DIFFERENT ICE CORE SITES

In this section we present an ensemble of implementations of the diffusion–densification model for various combinations of surface forcings that represent typical modern day conditions for a number of ice core sites on Greenland and Antarctica. The contours in the plot are generated by integration of Eq. (6) and expressed in m ice eq. The forcing for each ice core site is given in Table I and the results are shown in Fig. 2.

## IV. Estimation of $\sigma^2$ from the high resolution data set

In order to estimate the diffusion length value from high resolution water isotope data we minimize the 2-norm $\|P_s - \hat{P}_s\|$ where $\hat{P}_s$ is an estimate of the power spectral density of a high resolution $\delta^{18}$O data section and $P_s$ is a model description of the power spectral density.

The estimate of the power spectral density $\hat{P}_s$ of a $\delta^{18}$O dataset is obtained by the use of the Burg's spectral estimation method. The method fits an autoregressive model of order $\mu$ (AR-$\mu$) by minimizing the forward–backward prediction error filter (Hayes, 1996; Press et al., 2007; Andersen, 1974). For the theoretical model we have:

$$P_s = P_\sigma + |\hat{\eta}\,(k)\,|^2, \tag{19}$$

where $P_\sigma = P_0\, e^{-k^2\sigma_i^2}$ is the effect of the firn diffusion process with diffusion length $\sigma^2$. Regarding the noise, we find red noise described by an AR-1 process with an autoregressive coefficient $q_1 = 0.15$ to provide a good description of the noise signal we observe. The spectrum of this signal is of the form (Kay and Marple, 1981):

$$|\hat{\eta}(k)|^2 = \frac{\sigma_\eta^2 \Delta}{|1 + q_1 \exp(-ik\Delta)|^2}, \tag{20}$$

where $\sigma_\eta^2$ is the variance of the noise. The angular frequency $k = 2\pi f$ is in the range $f \in \left[0,\, \frac{1}{2\Delta}\right]$ defined by the Nyquist frequency and thus the sampling resolution $\Delta$. We vary the parameters $\sigma^2$, $P_0$, and $\sigma_\eta^2$ of the spectral model in order to minimize the misfit between $P_s$ and $\hat{P}_s$ in the least squares sense.

As it can be seen in Fig.3, it is the characterization of the spectrum as a whole that yields information on $\sigma^2$. It is thus not necessary to specifically study the relative attenuation of individual spectral peaks as for example the annual signal. This approach allows for a study of the diffusion signal even after the spectral signature of the annual signal diminishes below detection limit.

### *A. AR order selection*

An interesting feature of the Burg estimation method is that the order $\mu$ of the AR filter affects the spectral resolution of the spectral estimate (Hayes, 1996; Press et al., 2007). Low $\mu$ values result in smoother spectra with inferior spectral resolution, while higher order spectra show better performance in resolving neighboring spectral peaks. This can be seen in the spectral estimates presented in Fig.3 where we plot spectral estimates with $\mu = 30$ and $\mu = 40$. As described above, the goal of the $\sigma^2$ estimation is to characterize the overall shape of the spectrum. As a result, relatively low values of $\mu$ produce smooth spectra of relatively low spectral resolution and can be adequate for the purpose of our application.

We look into both the influence of the $\mu$ value on the $\sigma^2$ estimate by performing 41 power spectrum estimates with $\mu \in [40, 80]$. Possible interferences of spectral features due to longer scale climate variability that could have an effect on the estimation of $\sigma^2$ are also investigated with this test. In Fig.4 we show the mean value of the 41 spectral estimates before and after strain correction. The standard deviation of the estimated $\sigma^2$ for every depth is presented on the top subplot of the figure. It can be seen that on average the standard deviation is about 2 orders of magnitude lower than the absolute values of $\sqrt{\sigma^2}$ thus approximately in the 1% range. The low standard deviation of the 41 estimates suggests that a possible effect of spectral features due to low frequency climate variability is of second order. It also indicates that the selection of the AR order $\mu$, in Burg's spectral estimation is not a critical aspect of the estimation process.

### *B. Ice flow effects on the spectral estimation*

With depth increasing and due to the ice flow thinning, every discrete ice core sample cut at resolution $\Delta$ will represent an increasing number of years. This should not have an effect on the estimate of $\sigma^2$. As seen in Eq. (4) and of the MT, the diffusion process is seen as the convolution of the initial $\delta$ profile with a Gaussian filter. The convolution operation takes place in the $z$ domain. It conclusively follows that the transfer function of the diffusion process is a function of $k = 2\pi/\Delta$ and as a result estimation of $\sigma^2$ is performed using the power spectrum in the $k$ domain.

For the same reason, the correction term $\sigma_{dis}^2$, used in order to account for the diffusion imposed by the discrete sampling scheme is also a parameter that is constant with depth. Due to the ice layer thinning, percentage wise,

the discrete sampling correction increases with depth. It is also evident that with a constant value, $\sigma^2_{dis}$ represents an increasing number of years for higher depths. In Fig. 7, we illustrate the effect of this correction.

At increasing depths, $\sigma^2$ will be decreasing due to ice flow thinning. At lower $\sigma^2$ values, a spectrum estimate up to the Nyquist frequency $1/2\Delta$ will contain a decreasing part of the noise signal $|\hat{\eta}(k)|^2$. After a certain depth, the sampling resolution is not high enough to resolve the noise signal. The result of this effect is that the estimation of the $P_\sigma$ signal requires an assumption about $|\hat{\eta}(k)|^2$ and thus can limit the extend to which the diffusion technique can be applied to the deeper parts of the core.

In Fig. 5 we plot the expected diffusion length value assuming a simple case of constant temperature and accumulation rate at the surface and a certain ice layer thinning history. Then, based on this modeled diffusion length profile, in Fig. 6, we create a series of six power spectral densities for $z = 200, 600, 900, 1200, 1400 \text{ and } 1600\,\mathrm{m}$. The spectral models are calculated using 2 different sampling schemes, $\Delta_1 = 5\,\mathrm{cm}$ and $\Delta_2 = 2.5\,\mathrm{cm}$. The plots illustrate the effect of the ice layer thinning as well as the sampling resolution on the shape of the power spectral density. As depth increases, a progressively smaller portion of the noise signal is resolved. Conclusively, for the deeper parts of the core where the ice layer thinning has reduced the diffusion length, a higher sampling resolution ($\Delta < 2.5\,\mathrm{cm}$) is preferable for an accurate estimation of $P_s$ and subsequently $\sigma^2$ to be possible. For the NorthGRIP reconstruction we present here, we are able resolve the noise signal down to the depth of approximately 1450 m. For depths higher than 1450 m we make the simplest possible assumption that the noise level is equal to the average values we have observed in the Holocene section.

## V. Estimation of the uncertainties involved

In this section we assess the uncertainties involved in the estimation of the temperature. We identify two main sources of uncertainty. Those related to the parameters of the firn densification model and those related to the ice flow thinning. Each of these two sources of uncertainty is involved at different stages of the calculation and affect the estimation of the temperature in different ways.

Uncertainties related to the firn densification model have an impact on the inferred variability of the temperature signal. Centennial to millennial scale temperature signals as well as the amplitudes of climatic transitions will be affected by this type of uncertainty. On the contrary, the uncertainty associated with the ice thinning correction affects the slope of the signal. Relatively small variations in the thinning function can result in differences of several degrees in temperature. However this type of uncertainty can be minimized if estimates of temperature based on other proxies are available and can be used as tie points. In this case the firn diffusion technique can provide combined information on both the temperature history and the ice flow characteristics of the ice core site.

### *A. Firn densification model*

Uncertainties related to the densification model affect the estimation of the diffusion length $\sigma^2_{\mathrm{firn}}$ at the close–off depth. Hereby we examine the influence of four parameters involved in the densification–diffusion model. We run a set of sensitivity experiments where the four firn densification parameters are perturbed in order to create a family of 1000 implementations of the diffusion-densification model for each experiment. For all the following sensitivity tests we also consider the standard deviation of the diffusion length spectral estimate as calculated in section IV-A.

The first two parameters we consider are the surface and close–off densities $\rho_0$ and $\rho_{\mathrm{co}}$. We perform two sensitivity experiments where the values of $\rho_0$ and $\rho_{\mathrm{co}}$ are drawn from a Gaussian distribution with a defined mean and standard deviation (Table II). For the close–off density a value of $804 \pm 20\ \mathrm{kgm}^{-3}$ $(1\sigma)$ is used (Schwander et al., 1988; Jean-Baptiste et al., 1998; Johnsen et al., 2000). The range of values we choose for $\rho_{\mathrm{co}}$ brackets within $2\sigma$ the more extreme estimates of 775 and $840\ \mathrm{kgm}^{-3}$ shown in Scher and Zallen (1970) and Stauffer et al. (1985) respectively. For the surface density we use a value of $320 \pm 40\ \mathrm{kgm}^{-3}$ $(1\sigma)$, based on modern observations of the firn column density at NothGRIP. Previous high resolution density observations by Albert and Shultz (2002) for Summit, Greenland indicate that the surface density can vary within $\pm 50\mathrm{kgm}^{-3}$ of its mean value and as a result a $1\sigma$ of $40\ \mathrm{kgm}^{-3}$ assures that the Gaussian distribution of $\rho_0$ covers this range adequately in our sensitivity experiments.

We also include two parameters that describe the dependance of the densification rate to temperature. Based on Herron and Langway (1980)

$$\frac{\mathrm{d}\rho(z)}{\mathrm{d}t} = K(T) A^{\vartheta} \frac{\rho_{\mathrm{ice}} - \rho(z)}{\rho_{\mathrm{ice}}}, \tag{21}$$

where $K(T)$ is a temperature dependent Arrhenius–type densification rate coefficient described by:

$$K(T) = 11 \exp\left(-\frac{10160}{RT}\right) \quad \rho < 550 \text{ kgm}^{-3}, \tag{22}$$

and

$$K(T) = 575 \exp\left(-\frac{21400}{RT}\right) \quad \rho \geq 550 \text{ kgm}^{-3}. \tag{23}$$

In order to perturb the model we use the term $K'(t)$ in Eq. (21) where $K'(T) = fK(T)$ and $f = 1 \pm 0.2$ $(1\sigma)$. This results in a family of density profiles that are used for the diffusion length calculation. In Fig. 8 $1\sigma$ and $2\sigma$ intervals are illustrated together with firn density measurements from NorthGRIP.

The results of these sensitivity experiments are illustrated in Fig.9. Based on these results we conclude that using a fixed value for the surface and close–off densities is a plausible approach. The combined uncertainty of the $\rho_o$ and $\rho_{\text{co}}$ parameters is in the order of 1 K and thus the temperature history we infer is consistent over a wide range of densification parameter values.

### *B. Ice flow thinning uncertainties*

Uncertainties related to ice flow thinning depend on the accuracy of the ice flow model in inferring the ice thinning function. The value of the diffusion length of a layer at depth $z$, estimated from the spectral properties of a set of $\delta^{18}$O data needs to be corrected for ice flow thinning. An incorrectly estimated thinning function affects the inferred values of the diffusion length $\sigma^2_{\text{firn}}$ in a linear way as we show in Eq. (13) and (20) of the main text. As far as the inferred temperatures are concerned, the ice thinning function impacts the slope of the signal, thus presenting an increasing error with depth.

In Fig. 10 we performed the temperature calculation using six different scenarios for the ice thinning function $S(z)$. We assume the simple scenario of thinning function that varies linearly with depth and a value of $S(z = 2100 \text{ m})$ equal to $0.22, 0.24, 0.26, 0.28, 0.30, 0.32$. It is apparent that the change in temperature due to thinning function differences is significant. However the nature of this type of uncertainty, affecting only the slope of the signal, is such that unrealistic thinning function scenarios are relatively easy to disregard. Previous, estimates of temperature for any point in the climatic history of the record, obtained by other proxies, can be useful as they can help selecting a plausible scenario for the thinning function and thus fix the slope of the temperature signal inferred with the use of the firn diffusion method.

This characteristic, points to the usefulness of the method in providing combined paleotemperature and glaciological information. In this study the unrealistically high temperature values we inferred for the Holocene climatic optimum pointed to possible inaccuracies of the ice thinning function used for the estimation. When fixing the temperature gradient between the Holocene optimum and present conditions to be approximately 3 K, as inferred from previous studies (Dahl Jensen et al., 1998; Johnsen et al., 1995, 2001) we were able to propose a more likely scenario for the ice thinning function and as a result the accumulation rate history. The temperature reconstruction using the proposed ice thinning function is presented in red color in Fig. 10.

## REFERENCES

Albert, M. R., Shultz, E. F., May 2002. Snow and firn properties and air-snow transport processes at summit, greenland. Atmospheric Environment 36 (15-16), 2789–2797.

Andersen, N., 1974. Calculation of filter coefficients for maximum entropy spectral analysis. Geophysics 39 (1), 69–72.

Blicks, H., Dengel, O., Riehl, N., 1966. Diffusion von protonen (tritonen) in reinen und dotierten eis-einkristallen. Physik Der Kondensiterten Materie 4 (5), 375–381.

Dahl Jensen, D., Mosegaard, K., Gundestrup, N., Clow, G. D., Johnsen, S. J., Hansen, A. W., Balling, N., Oct. 1998. Past temperatures directly from the greenland ice sheet. Science 282 (5387), 268–271.

Delibaltas, P., Dengel, O., Helmreich, D., Riehl, N., Simon, H., 1966. Diffusion von $^{18}$O in eis-einkristallen. Physik Der Kondensiterten Materie 5 (3), 166–170.

Hall, W. D., Pruppacher, H. R., 1976. Survival of ice particles falling from cirrus clouds in subsaturated air. Journal of the Atmospheric Sciences 33 (10), 1995–2006.

Hayes, M. H., 1996. Statistical digital signal processing and modeling. John Wiley & Sons.

Herron, M. M., Langway, C. C., 1980. Firn densification - an empirical-model. Journal Of Glaciology 25 (93), 373–385.

Itagaki, K., Feb. 1967. Self-diffusion in single crystal ice. J. Phys. Soc. Jpn. 22 (2), 427–431.

Jean-Baptiste, P., Jouzel, J., Stievenard, M., Ciais, P., May 1998. Experimental determination of the diffusion rate of deuterated water vapor in ice and application to the stable isotopes smoothing of ice cores. Earth And Planetary Science Letters 158 (1-2), 81–90.

Johnsen, S. J., Clausen, H. B., Cuffey, K. M., Hoffmann, G., Schwander, J., Creyts, T., 2000. Diffusion of stable isotopes in polar firn and ice. the isotope effect in firn diffusion. In: Hondoh, T. (Ed.), Physics of Ice Core Records. Hokkaido University Press, Sapporo, pp. 121–140.

Johnsen, S. J., Dahl Jensen, D., Dansgaard, W., Gundestrup, N., Nov. 1995. Greenland paleotemperatures derived from grip bore hole temperature and ice core isotope profiles. Tellus Series B-Chemical And Physical Meteorology 47 (5), 624–629.

Johnsen, S. J., DahlJensen, D., Gundestrup, N., Steffensen, J. P., Clausen, H. B., Miller, H., Masson-Delmotte, V., Sveinbjornsdottir, A. E., White, J., 2001. Oxygen isotope and palaeotemperature records from six Greenland ice-core stations: Camp Century, Dye-3, GRIP, GISP2, Renland and NorthGrip. Journal Of Quaternary Science 16 (4), 299–307.

Kay, S. M., Marple, S. L., 1981. Spectrum analysis - a modern perspective. Proceedings Of The Ieee 69 (11), 1380–1419.

Majoube, M., 1971. Fractionation in O-18 between ice and water vapor. Journal De Chemie Physique Et De Physico-Chimie Biologique 68 (4), 625–&.

Merlivat, L., Jouzel, J., 1979. Global climatic interpretation of the deuterium-oxygen 18 relationship for precipitation. J. Geophys. Res. 84(C8), 5029–5033.

Merlivat, L., Nief, G., 1967. Fractionnement isotopique lors des changements detat solide-vapeur et liquide-vapeur de leau a des temperatures inferieures a 0 degrees c. Tellus 19 (1), 122–127.

Murphy, D. M., Koop, T., Apr. 2005. Review of the vapour pressures of ice and supercooled water for atmospheric applications. Quarterly Journal Of The Royal Meteorological Society 131 (608), 1539–1565.

Press, W. H., Teukolsky, S. A., Vetterling, W. T., Flannery, B. P., August 2007. Numerical Recipes: The Art of Scientific Computing. Cambridge University Press.

Ramseier, R. O., 1967. Self-diffusion of tritium in natural and synthetic ice monocrystals. Journal Of Applied Physics 38 (6), 2553–2556.

Scher, H., Zallen, R., 1970. Critical density in percolation processes. Journal of Chemical Physics 53 (9), 3759–3761.

Schwander, J., Stauffer, B., Sigg, A., 1988. Air mixing in firn and the age of air at pore close-off. Annals Of Glaciology 10, 141–145.

Stauffer, B., Schwander, J., H., O., 1985. Enclosure of air during metamorphosis of dry firn to ice. Annals of Glaciology 6, 108–112.

| Site | Location | Accum. Rate [myr$^1$] | Temperature [C] | $\sigma^2_{18}$ [m] |
|---|---|---|---|---|
| Dome C | 75°06′S 123°21′E | 0.027 | -54.5 | 0.067 |
| GISP2 | 72°36′N 38°30′W | 0.24 | -31.4 | 0.079 |
| GRIP | 72°35′N 37°38′W | 0.23 | -31.7 | 0.0795 |
| NEEM | 77°45′S 51°06′W | 0.2 | -30 | 0.088 |
| NorthGRIP | 75°10′N 42°32′W | 0.207 | -32 | 0.081 |
| SipleDome | 81°40′S 148°46′W | 0.087 | -25 | 0.145 |
| South Pole | 90°S 00° | 0.076 | -51 | 0.054 |
| Vostoc | 78°27′S 10°51′E | 0.024 | -55.5 | 0.067 |

TABLE I: Surface forcing used for the diffusion length calculations in Fig. 2.

| | $f_o$ | $f_1$ | $\rho_0$ | $\rho_{co}$ |
|---|---|---|---|---|
| Experiment 1 | 1 | 1 | 320 kgm$^{-3}$ | $804 \pm 20$kgm$^{-3}$ |
| Experiment 2 | 1 | 1 | $320 \pm 40$ kgm$^{-3}$ | 804 kgm$^{-3}$ |
| Experiment 3 | $1 \pm 0.2$ | $1 \pm 0.2$ | 320 kgm$^{-3}$ | 804 kgm$^{-3}$ |
| Experiment 4 | $1 \pm 0.2$ | $1 \pm 0.2$ | $320 \pm 40$ kgm$^{-3}$ | $804 \pm 20$ kgm$^{-3}$ |

TABLE II: Summary of the sensitivity experiments run

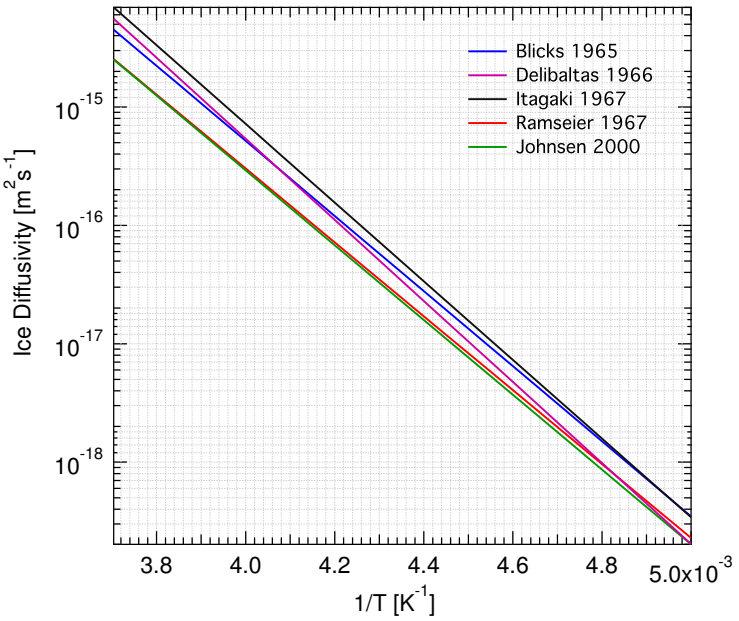


Fig. 1: Ice diffusivity parametrizations based on isotopic probe experiments for the temperature range 200 – 270 K

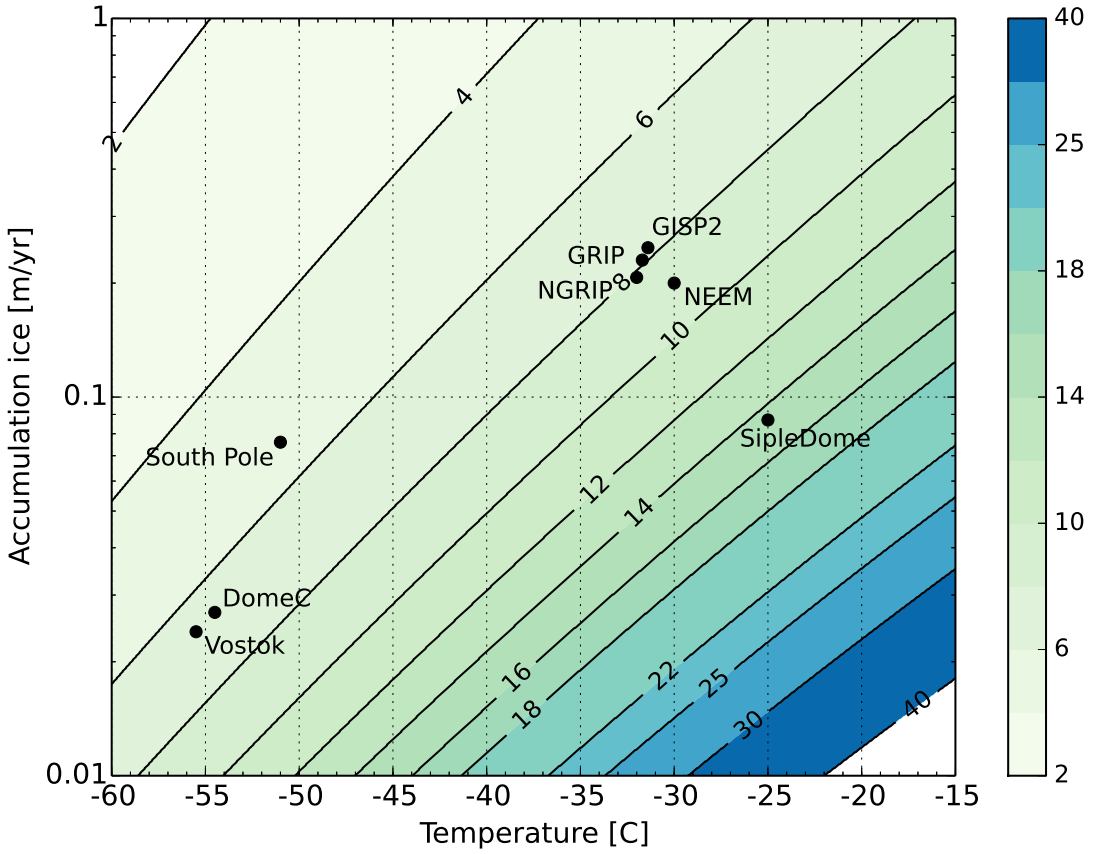


Fig. 2: Calculation of $\sigma^2_{18}$ for the close–off density of $\rho_{\text{co}} = 804.3$ kgm$^{-3}$ in m of ice equivalent. We used the same surface density $\rho_o = 330$ kgm$^{-3}$ for all sites.

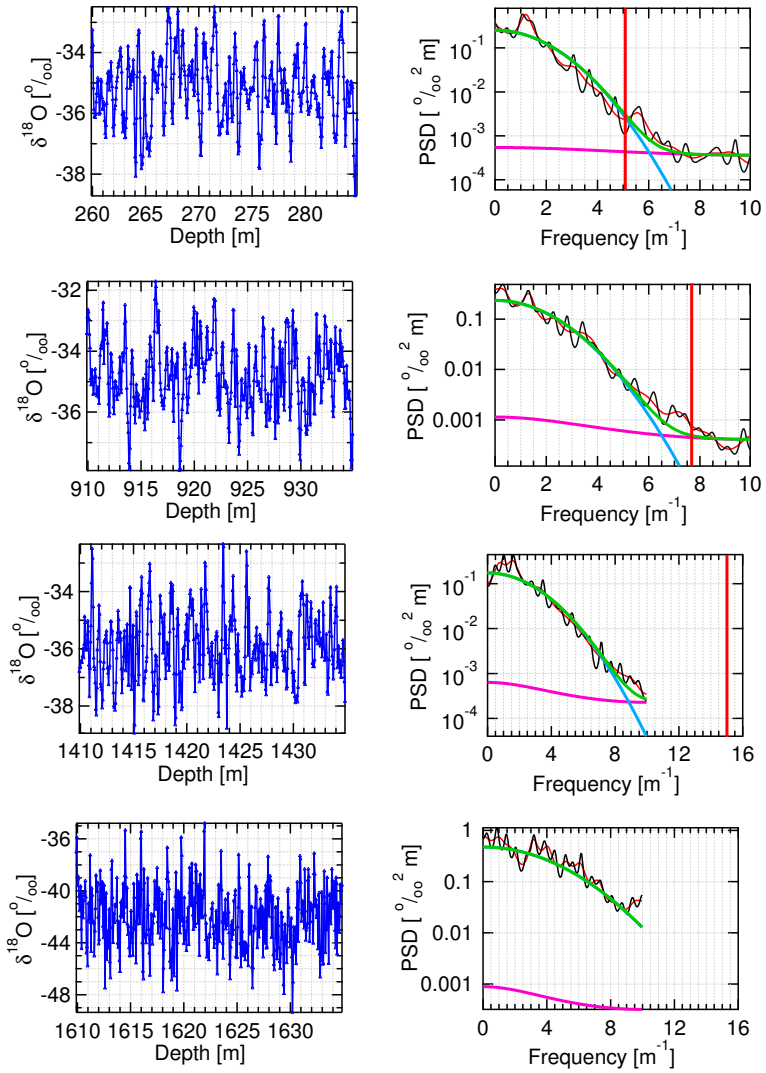


Fig. 3: Examples of raw $\delta^{18}$O data and estimated power spectral densities $\hat{P}_s$ for four different depth intervals using $\mu = 30$ (red spectra) and $\mu = 40$ (black spectra). The power spectral model is illustrated; $P_s$ in green, $P_\sigma$ in cyan and $|\hat{\eta}(k)|^2$ in pink. The red vertical line in the top three plots indicates the approximate position of the frequency representing the annual layer thickness. For the bottom plot this frequency is $\approx 40\,\mathrm{m}^{-1}$ and omitted from the plot.

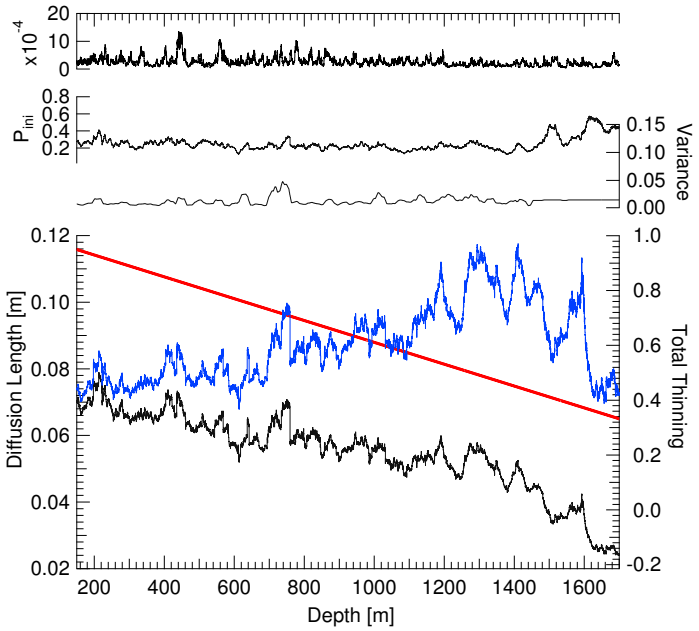


Fig. 4: Vertical profiles of $\sigma_{\rm firn}$, $S(z)\sigma_{\rm firn}$, $\sigma_{\rm ice}$ and $\sigma_i$ For the calculation of $\sigma_{\rm firn}$ the parameters we used for the H–L model were: $P = 0.7$ Atm, $\rho_0 = 330\ {\rm kgm}^{-3}$, $\rho_{\rm CO} = 804.3\ {\rm kgm}^{-3}$, $T = 242.15$ K, and $A = 0.2\ {\rm myr}^{-1}$ ice eq. Top plot: Standard deviation of the 41 estimates of the diffusion length for every depth in m ice eq.

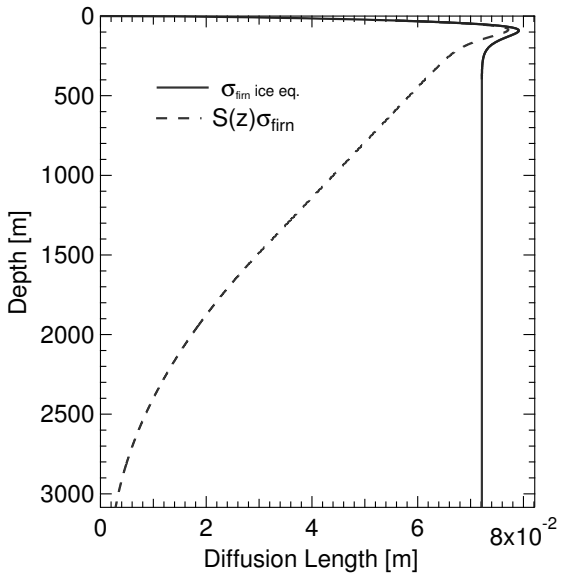


Fig. 5: Effect of the ice layer thinning on the value of the diffusion length. For the calculation of $\sigma_{\rm firn}$ the parameters we used for the H–L model were typical of Holocene conditions for the NorthGRIP site: $P = 0.7$ Atm, $\rho_0 = 330\ {\rm kgm}^{-3}$, $\rho_{\rm CO} = 804.3\ {\rm kgm}^{-3}$, $T = 242.15$ K, and $A = 0.2\ {\rm myr}^{-1}$ ice eq.

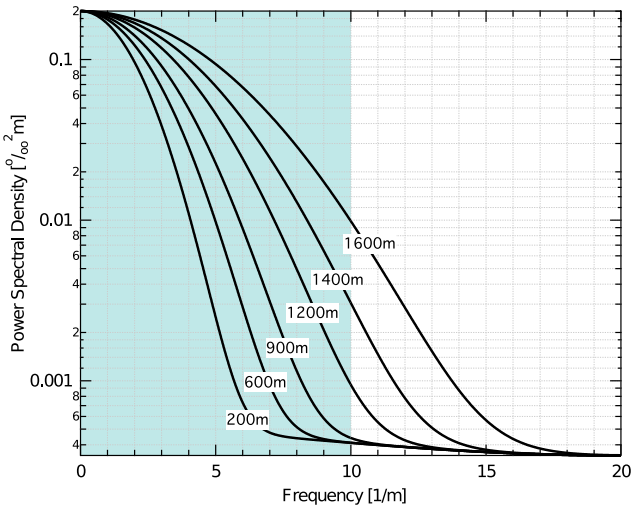


Fig. 6: Modeled power spectral densities for 6 different depths using diffusion length values from the calculation of Fig. 5 (Note that all plots represent identical accumulation rate and temperature forcing at the surface). We use the spectral model as in Eq. 19 with $q_1 = 0.15, P_{ini} = 0.2$. The highlighted area represents the expected spectra for the case of $\Delta = 5\text{cm}$ $\left(f_{Nyq} = 10\,\text{m}^{-1}\right)$ while the full range of the modeled spectra represents the case with $\Delta = 2.5\,\text{cm}$ $\left(f_{Nyq} = 20\,\text{m}^{-1}\right)$.

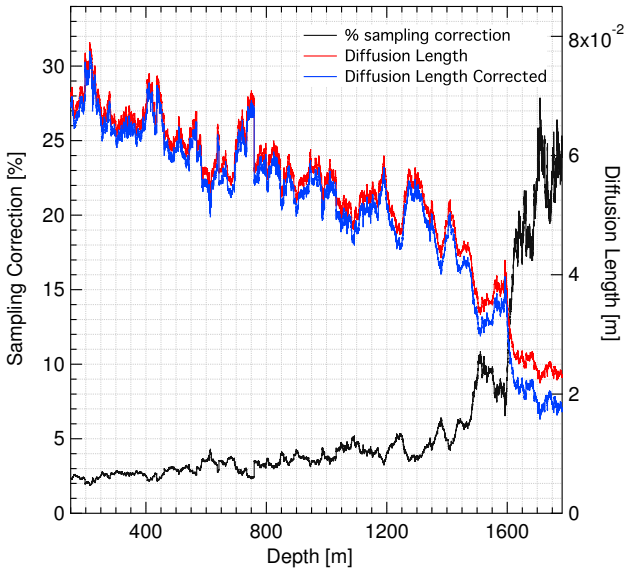


Fig. 7: Discrete sampling correction

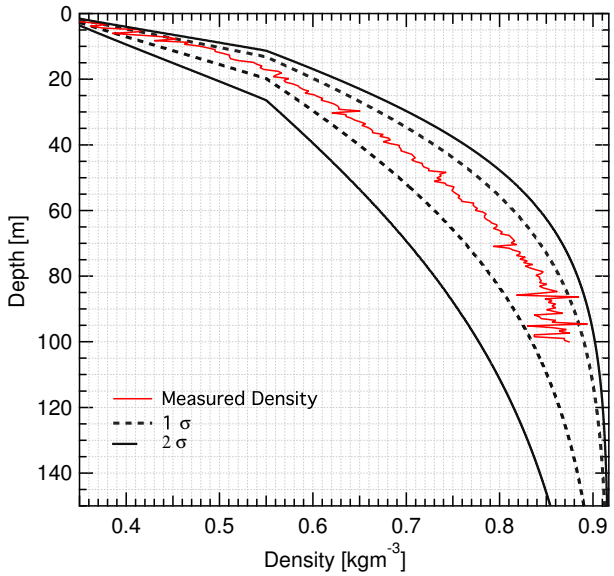


Fig. 8: Firn density measurements from NorthGRIP (red) compared to implementations of the H-L densification model with varying values of $f$. Solid and dashed curves illustrate the range of $1\sigma$ and $2\sigma$ respectively.

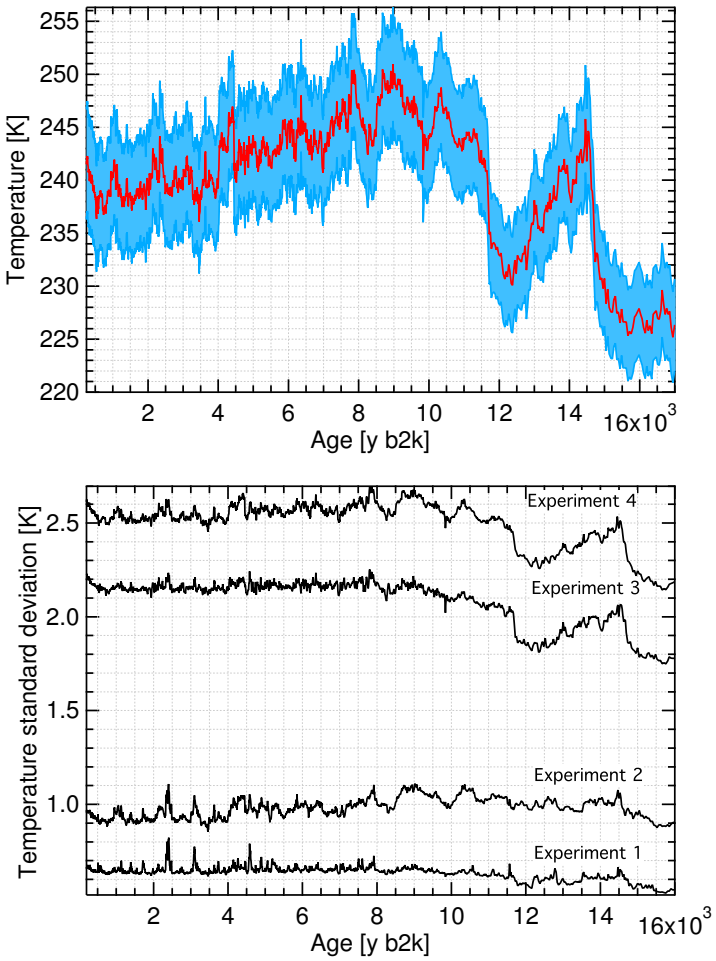


Fig. 9: Sensitivity tests results. The top panel illustrates the mean temperature history as calculated from Experiment 4 (all parameters varied) bracketed by the 95% confidence interval estimated with the sensitivity test. In the bottom panel we present the value of the standard deviation ($1\sigma$) for each sensitivity test.

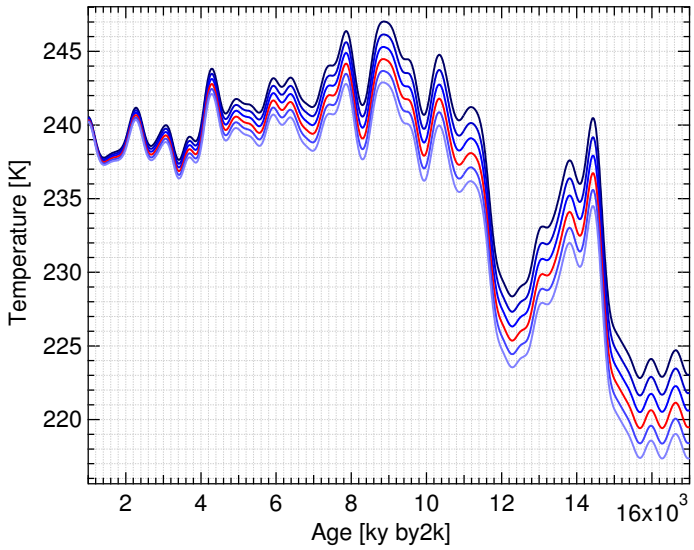


Fig. 10: Ice thinning uncertainty illustrated. Temperature reconstructions for NorthGRIP using (from high to low) $S(2100m) = 0.22, 0.24, 0.26, 0.28, 0.30, 0.32$. Records filtered with a 500y low-pass filter.